





Analysis of Shielding Gases Influences 304 Gas Metal Arc Welding Microstructure, Weld Geometry, and Mechanical Properties



Dauod S. Dauod¹, Kadhum Jasem Wade², Mohammed Sabeeh Mohammed^{3*}, Hasan Shakir Majidi⁴

¹ Production Engineering and Metallurgy Department, University of Technology-Iraq, Baghdad 10066, Iraq

² Institute of Technical Trainers Preparing, Middle Technical University, Baghdad 10066, Iraq

³ Training and Workshops Center, University of Technology- Iraq, Baghdad 10066, Iraq

⁴ Department of Chemical Engineering and Petroleum Industries, Al-Mustaqbal University, Hillah 51001, Babylon, Iraq

Corresponding Author Email: mohammed.s.mohammed@uotechnology.edu.iq

Copyright: ©2024 The authors. This article is published by IIETA and is licensed under the CC BY 4.0 license (<http://creativecommons.org/licenses/by/4.0/>).

<https://doi.org/10.18280/rcma.340405>

ABSTRACT

Received: 24 February 2024

Revised: 22 April 2024

Accepted: 22 June 2024

Available online: 27 August 2024

Keywords:

transition zone, sensitization, martensite, cooling rate, fusion boundary

Shielding gases had considerable significance in welding metal protection from contamination during welding. Welding protection gas is essential in welding joint quality, connected to the arc characteristics and weldment microstructure. Understanding the influence of welding shielding gas in different metal welding processes is extremely important, and many research papers and experiments have been performed. The current study objective is to analyse and summarize shielding gas variations' effects on welding joint bead geometry, dilution percentage, joint soundness, and microstructure by examining the impacts of different protection gas combinations on AISI 304 stainless steel MIG welding. Three AISI 304 weldment samples were welded with MIG technology and 308L filler wire, and three different gas mixtures as protection gas; the dilution percentage for every sample was calculated to evaluate gas mixture influence on heat concentration on welding zone geometry calculation—ferrite percentage and calculated to estimate and predicate the final welding microstructure and texture. An optical microscope and SEM were employed to reveal weldment microstructure, welding porosity, and defects and study their impact on mechanical properties. Vickers microhardness and tensile tests were done to record gas mixture effects on welding zone hardness and strength. Variation in gas mixture effects on weldments' corrosion resistance was recorded using a corrosion test on every welding sample. These research results can be used as guidelines to achieve the required welding quality in practical welding and provide an excellent foundation for understanding and solving shielding gas issues in the metal welding industry and evaluating welding protection gas mixtures' productivity and quality. The heat input of the three samples is equal due to the use of the same voltage, current, and travel speed; for that, we need to profoundly analyse the weldments microstructure and analyse the impacts of variation in microstructure, which resulted from protection gas mixture effects on the cooling rate on weldments mechanical properties. It fits with the requirements of design criteria.

1. INTRODUCTION

In the industry sector, especially in automobile and railway equipment production, stainless steel has significant applications in final product manufacturing. Welding and usually Gas Metal Arc Welding (GMAW) technology is essential due to its advantages and economic aspects [1]. Stainless steel or corrosion-resistant steel are iron-based alloys that have excellent corrosion resistance. Stainless steel is widely used in food vessels, kitchen equipment, transportation staff, and buildings due to its distinguished corrosion resistance and shining look; 304 stainless steel is commonly used for manufacturing since it is considered excellent when it forms the required design [2]. Austenitic types of stainless steels are regarded as one perfect option in metals selection for

many applications; austenitic types combine good corrosion resistance and excellent toughness and strength, especially with L grades, which are distinguished by low carbon to prohibit intergranular corrosion and ameliorate weldability. Also, this grade indicates nitrogen addition to level up mechanical strength [3]. According to structure design, stainless steel requires welding assembly, for example, stainless steel pipes, automotive exhaust gas systems, and chemical industrial equipment repair [4]. When good formability and high corrosion resistance are demanded, AISI 304L austenitic stainless steel would be the best choice, like chemical plants' cylindrical components with domes and toro spherical [5]. Stainless steel is welded with the MIG/MAG process using either spray, gobbler, or short-circuiting metal transfer. Austenitic 304 stainless steel has excellent

formability and invariably improves ultimate and allowable tensile stress. Its market has experienced continuous growth due to its highlight characteristics and perfection in equipment manufacturing of these materials. MIG/MAG welding technology is a commonly used process in almost all heavy metal industries of this metal. When there are increasing costs, these techniques are also considered when increasing productivity is a priority [6]. Welding shielding gas is essential in MIG/MAG welding; protective gas influences fusing joint quality, appearance, welding speed, and production process costs. Nowadays, gas arc welding processes deal with different welding shielding gases. Gas suppliers' companies mainly produce welding gas mixtures to lower welding gas prices, but this should not affect the quality of welding and weldment design criteria. Previous research and gas suppliers and production organizations' study results about this subject reveal many problems with many gas mixture formulas. Still, all of it only discussed how welding gas influenced the reduction of welding joint mechanical properties, porosity, and cracks issues without deeply analysing weldment microstructures to understand the foundations of the problem. In this research, welding is done with the Gas Metal Arc Welding (GMAW) technique with different inert protection gas mixtures to realize the consequences of welding gas mixtures on weldments and welding zone properties.

2. LITERATURE REVIEW

Previous research on 304 stainless steels welded by the MIG welding process and Argon with 1.5% Hydrogen as shielding gas mixture by Gülenç et al. [7] shows good tensile strength with 240A welding current specimen. They are also increasing the welding penetration profile width and depth marked. Results of Boiko and Avisans [8] study showed that the economical way to prevent welding joint microalloying elements is carbon dioxide increasing in shielding gas mixture with oxygen-involved shielding gas mixtures of 99.95% purity Argon gas, 90% Argon, and 10% carbon dioxide gas mixture, 90% Argon and 5% carbon dioxide and 5% oxygen gas mixture respectively used in these experiments. MIG welding of stainless steel employing Argon (Ar), Nitrogen (N₂), Argon mixed with Nitrogen, and a mixture of Argon, Nitrogen, and 10% Hydrogen (H₂) as purging gases investigated by Taban et al. [9], research results reveal increases in welding effectiveness and fewer defects produced during welding with this mixture, and explain that one of the essential advantages of purging gas in welding is decreased heat effects and ferromagnetic layers formation which appeared as coloured oxide films lighter in colour than welding without protection gas. Stainless steel welding is critical because of its low thermal conductivity and high thermal expansion, which cause serious distortion issues when using fusion welding technology. To avoid distortion, welding must be carried out at a lower allowable current, providing good penetration and fluidity of welding metal to fulfil good mechanical and chemical properties. The filler wire diameter is also based on austenitic stainless steel AISI 304 earlier welding experiments done by Salleh et al. [10] on different sizes of welding filler wires; results show energy absorbed reduced when 1.2 mm filler wire is used. Generally, 1.2 mm welding filler wire required the highest energy compared with 1.0 mm and 0.8 mm filler wire when welding arc voltage change. Welding process parameters had essential effects on MIG/MAG

welding, welding current, voltage, and shielding gas pressure. Kishore et al. [11] research demonstrated that these parameters would command welding metal fluidity and penetration and should be carefully selected in the MIG welding experiment. Welding parameters in this study were set up to obtain the spray transfer mode of molten metal, which, according to Palani and Murugan [12], previous work produced the best weld geometry and excellent dynamic characteristic quality, responsible for good welding joints. Welding procedure parameters such as voltage (V), current (A), speed (M/Min), and gas flow rate (L/Min) in this experiment had detrimental effects on s/n ratio and ultimate tensile strength (UTS) at specific range set according to the study of Utkarsh et al. [13] which explains in details the impacts of these parameters on welding joint quality. Impacts of hydrogen addition in shielding gas to argon when stainless steels and high alloy steel welding demonstrated by Tusek and Suban [14], argon and hydrogen mixture preferred to employ as shielding gas in MIG and TIG welding processes, in nickel-copper, stainless steel and nickel-based alloys these shielding gases would produce joints with good results. Althouse et al. [15] study results reveal that this mixture's main advantage is permitting increasing welding speeds. Still, at the same time, hydrogen is not preferred on most metals due to its hydrogen crack formation in welds microstructure. Molten material volume increased in the welding pool with hydrogen addition to the protection gas mixture; the investigation results of Lowke et al. [16] explain this significant increase due to the argon/hydrogen mixture's high thermal conductivity at hydrogen molecules dissociate temperatures.

This experiment aims to deeply analyse welding zone microstructures, to find out the influence of welding gas composition on stainless steel weldment mechanical properties and corrosion resistance ability using MIG welding, and to give the best opportunities for gas production companies and suppliers to choose the best MIG/MAG shielding gas suitable with production plants and required quality of final welding joint according to design requirements.

3. EXPERIMENTAL WORK

In this experimental study, 8 mm thickness 304 austenitic stainless-steel specimens shown in Figure 1 were welded to each other with MIG welding technology using 1.2 mm welding filler wire.



Figure 1. Welding test plate configuration

The composition of AISI 304L is tabulated in Table 1, and the chemical composition of the welding filler wire is shown in Table 2.

Table 1. AISI 304L base metal chemical composition

C	Ni	Cr	Mn	Co	Si	Cu	Mo	P	Fe
0.01	8.1	18.4	1.4	0.09	0.4	0.2	0.2	0.028	Balance
8	4	6	7	1	9	8	4	7	e

Table 2. ER 308L filler chemical composition

C	Ni	Cr	Mn	Co	Si	Cu	Mo	P	Fe
0.02	9.81	20.11	1.78	----	0.51	----	0.13	----	Balance
				-		-		-	

Stainless steel samples were prepared with 150×90 mm dimensions using a wire cutting machine and then chamfered with 30 and placed adjacent to each other with a 2 mm open root distance between them above the copper plate; welding was carried out with ESAB MIG welding machine and completed with two welding passes and cooled in air after each pass. Welding uses three different shielding gases: pure argon of 99.95% purity, argon with carbon dioxide of 75:25, and argon with hydrogen of 95:5 ratios. After welding, the area is immediately cleaned with a steel wire brush. Now, welding is done with the backhand technique, at the flat position and butt joint, for all three joints, weld parameters keeping constant as shown in Table 3. The spatters present near the weld area were

Table 3. MIG welding parameters

S No.	Current A.	Voltage V.	WS mm/min	WFS m/min	HI kJ/mm	Gas mixture	GFR L/min
W1	250	29.5	500	8.5	0.885	Ar + 5% H ₂	16
W2	250	29.5	500	8.5	0.885	Pure Ar	16
W3	250	29.5	500	8.5	0.885	Ar + 25% CO ₂	16

WS=welding speed WFS=wire feed speed GFR=gas flow rate HI=heat input (V*A*60)/(WS mm/min)

3.2 Metallography

Welded metal microstructure samples of welding zone, HAZ, and base metal cutting by EDM techniques to the desired dimensions and then grinding with emery papers starting from 200 until the mirror face polished by diamond pates then etched with three parts of HCL, two parts of acetic acid, 1-part HNO₃, and two drops glycerol for 5 seconds to examine the microstructure. Light OM (model BMM-2000) device used in microstructural examination with different magnifications.

3.3 Scanning electron microscopy (SEM) and electron diffraction scanning (EDS)

SEM test was employed to examine the microstructure in deep detail. AISI 304 base metal, welding metal zone, and HAZ SEM samples for the three gas mixture experiments cutting with a wire cutting machine, then polishing and followed by chemical etching. EDS analysis discloses element depletion and transformation between the welding zone and HAZ and reveals gas mixture impacts on element disruption.

3.4 Dilution calculation

Evaluation of three gas mixtures weld metals chemical compositions done by calculating the dilution percentage

removed using a chisel hammer. The joints were visually examined for surface defects like blowholes, porosity, surface cracks, undercuts and penetration, etc.

3.1 Welding procedure

The welding was achieved using an EASB fully thyristorised (made in Sweden) air-cooled MIG/MAG machine with (DCEP) polarity. Maximum operation current is 400 A with 50-volt open circle voltage (OCV) and 20m/min wire feed speed (WFS). A stationary welding table is used to support weldment samples. The welding torch was mounted by hand above the welding work table to adjust the required distance between the welding torch nozzle and weldment plates and fix the torch angle. MIG Welding parameters employed to manufacture welding joints are illustrated in Table 3. Weldment parts arrangements are acquired by tacking the plate's edges flat to avoid weldment distortion. Butt joints with chamfered edges with 30° for each side and a 2 mm root gap for the MIG welding joint. Spray mode metal transfer was chosen to complete welding joints. To obtain welding operation mode, operation current and voltage are monitored with an oscilloscope through all welding sequences. Pure argon with 20% CO₂ and 5% H₂ shielding gas mixtures were used during welding experiments. The necessary configuration has been taken to avoid welding thermal distortion by exercising strong clampers. The welded joint's soundness was examined with radiography testing to ensure welding quality.

(DL%) from weld joints' geometrical characteristics like weld deposit total area (A_{WD}), weld reinforcement area (A_{TR}), root reinforcement (A_{RR}), base metal fusion area (A_{BF}), and finally root gap area (A_{RG}), as schematically illustrated in Figure 2. calculation of A_{WD}, A_{BF}, and DL percentage founded by employing the following Eqs. (1) and (2) [17]:

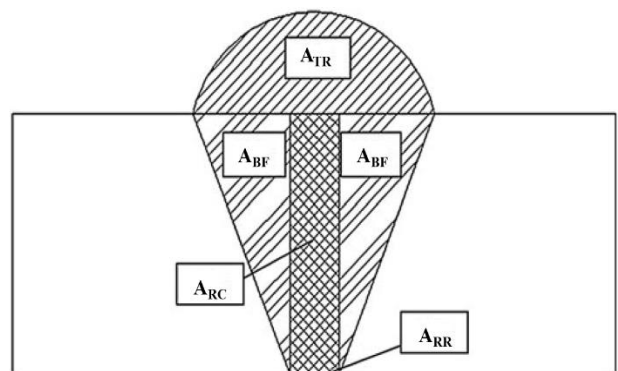


Figure 2. Weldment joint dilution calculation schematic view sample

$$AWD = ARG + ATR + ABF + ARR \quad (1)$$

$$DL\% = ABF / AWD \times 100\% \quad (2)$$

3.5 SFE calculation, martensite transformation (MT) temperatures and Cr-Ni equivalents

Compositions of welding metal which estimated from dilution calculations are used in chromium equivalent (Cr_{eq}) and nickel equivalent (Ni_{eq}) calculations employing the following Eqs. (3) and (4) [18]:

$$Cr_{eq} = Cr\% + Mo\% + 0.7Nb\% \quad (3)$$

$$Ni_{eq} = Ni\% + 35C\% + 20N\% + 0.25Cu\% \quad (4)$$

where, A_3 is γ to α phase pure iron transformation temperature, and A_E is fictional phase γ to ϵ transformation temperature, about 390K (18). SFE calculated with Rhodes and Thompson developed Eq. (5) [19], as follows:

$$SFE(mJ/m^2) = 1.2 + 1.4\%Ni + 0.6\%Cr + 7.7\%Mn - 44.7\%Si \quad (5)$$

3.6 Grain size estimation and ferrite value measurement

According to ASTM E1382, the grain size of code weld metals was evaluated and estimated from the optical micrographs by a linear intercept method, and image analyzing software was used for these calculations. Five readings were reported, and the average was taken according to the ASTM code. The Feritscope FMP30 method was used to evaluate the ferrite percentage of three gas mixture welding zone samples; ten readings on average for each weld metal were reported to achieve accurate measurements.

3.7 Vickers microhardness

welding joint and HAZ metallographic specimen with flat position used to microhardness survey across HAZ and welding zone for each one of three-gas mixture welded samples with Vickers microhardness testing machine employed 100gf load and 500 μ m space between marks.

3.8 Tensile testing

Three tensile test specimens were prepared by CNC machine with standard dimensions on the authority of ASTM E8 M-04 code, as illustrated in Figure 3. Smooth transverse edges of tensile test samples manufacturing to evaluate transverse tensile characteristics of gas mixtures welding joint. The specimens were tested with a 100kN electromechanical controlled testing machine, and three readings were reported for each gas mixture sample.

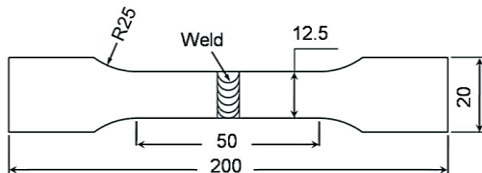


Figure 3. Tensile test welded joint samples dimensions

3.9 Microstructures evaluation

The microstructure of welding zone metals and transition zone welded with 5% H_2 + Ar and 240 Amp welding currents

illustrated in Figures 4(a) and (b) shows weld metal with austenitic structure utterly different from base metal microstructure.

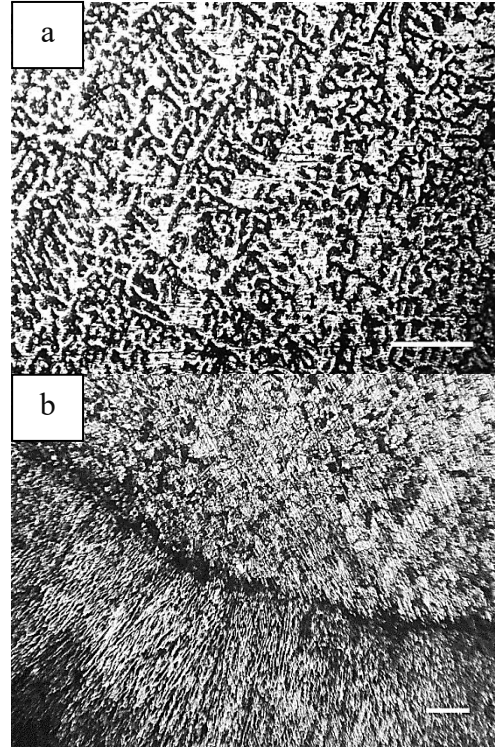
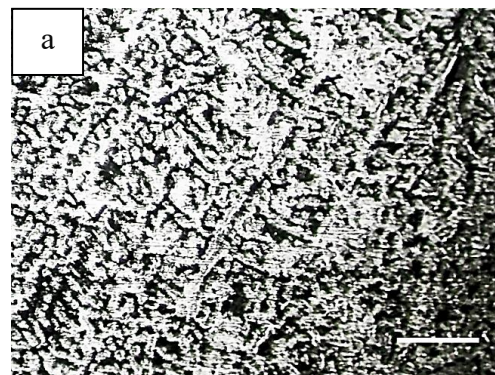


Figure 4. (a) Weld metal microstructure with 5% H_2 + Ar; (b) Transition zone

Weld metals and transition zone microstructure under pure Ar shielding, as seen in Figures 5(a) and (b), show weld metal microstructure similar to the microstructure in Figure 4, which is welded with 5% H_2 + Ar shielding gas. Still, the microstructure is rougher than Figure 4. Figure 5(b) reveals the transition zone between weld metal and parent metal; this transition zone is not smooth but visible. The orientation of grains in the welding zone metal was noticed to be with the heating flow direction. This orientation is also marked in literature [20, 21]. The weld metal and transition zone microstructure in Figures 6(a) and (b) of the welded sample under 75% Ar with 25% CO_2 shielding gas mixture reveals an utterly different microstructure from previous shielding gases. Microstructure pictures show dendritic microstructure in a welding zone containing austenite with deposit martensite at grain boundaries. The transition zone microstructure in Figure 6(b) illustrates an apparent transition zone with a heavy martensite structure.



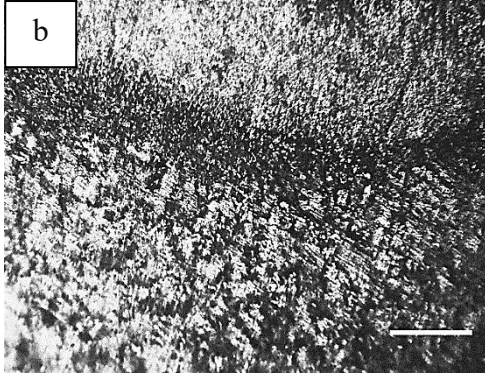


Figure 5. (a) Weld metal microstructure with pure Ar; (b) Transition zone

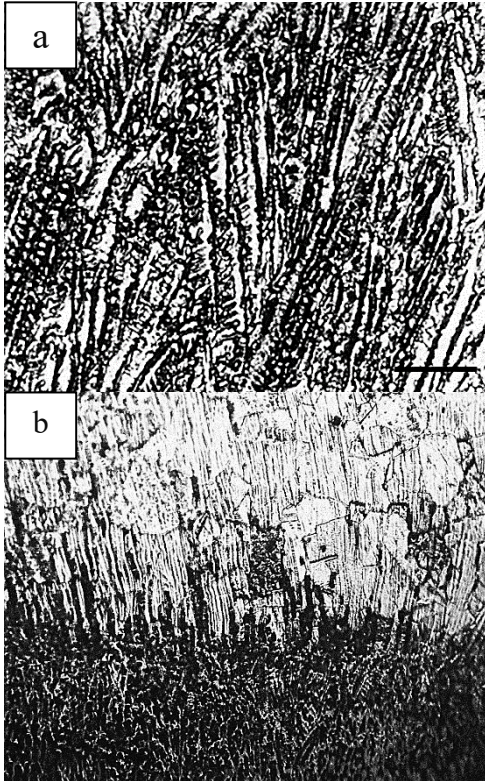


Figure 6. (a) Weld metal microstructure with 25% CO₂ + Ar; (b) Transition zone

3.10 SEM and EDS evaluation

W1 SEM of the welded sample under pure Ar shows lath and skeletal embedded ferrite microstructure in the austenitic matrix as intergranular ferrite.

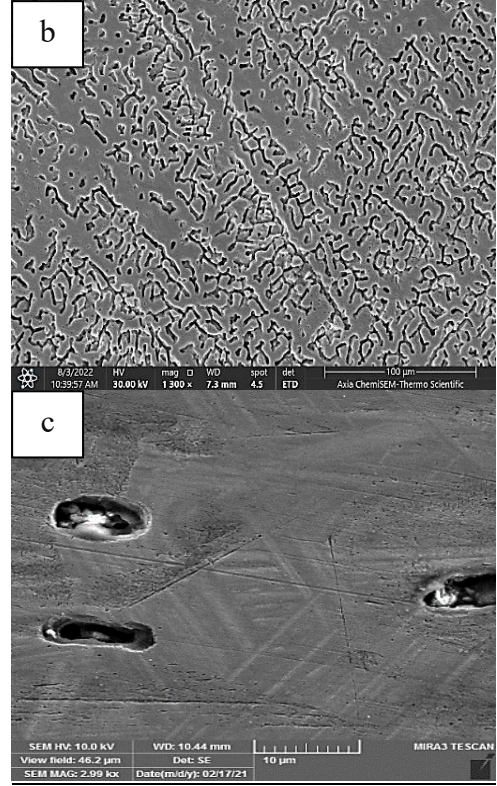
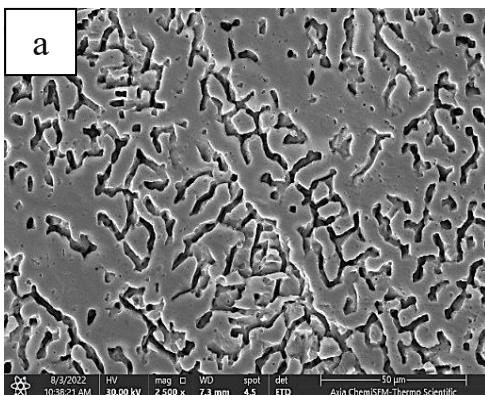


Figure 7. (a) Weld metal microstructure SEM with 5% H₂ + Ar; (b) Weld metal microstructure SEM with pure Ar; (c) Weld metal microstructure SEM with 25% CO₂ + Ar

Figure 7(a) reveals weld metal with δ -ferrite intergranular nature and high lath δ ferrite constrain in W1 welding metal, W2 SEM of welded sample under pure 5% H₂ + Ar illustrated almost identical structure of W1 as in Figure 7(b), W3 weld metal microstructure welded with 25% CO₂ + Ar shown completely different microstructure with obvious martensite needles and porosity as seen in Figure 7(c).

3.11 Welding arc heat flux density distribution model

The computer simulation model in Figures 8(a) to (c) of welding arc heat flux density distribution for the three welding shielding gases used in this study shown increasing in welding arc heat flux density when a small amount of H₂ gas add to protection gas, this means the welding heat efficiency will increases. It also demonstrated the 25% CO₂ addition effect on welding arc heat flux density. According to an earlier study, welding protection gas composition deeply affects welding heat efficiency and welding geometrical parameters and can estimated by the following Eq. (6) [22]:

$$q = q_{max} \text{EXP}(-kr^2) \quad (6)$$

where, q is the heat flux density, q_{max} is the maximum heat flux density, k is the heat concentration factor, and r is the radial distance from the arc axis. When using arc welding, heating power is considered a kind of electrical energy, so that the following Eq. (7) can be applied [22]:

$$q = \eta_h \times UI \quad (7)$$

where, η_h is the heating efficiency, U is the welding voltage,

and I is the welding current. Heating efficiency can be calculated using the following Eq. (8):

$$\eta_h = \sqrt{Jq_{max}} / kUI \quad (8)$$

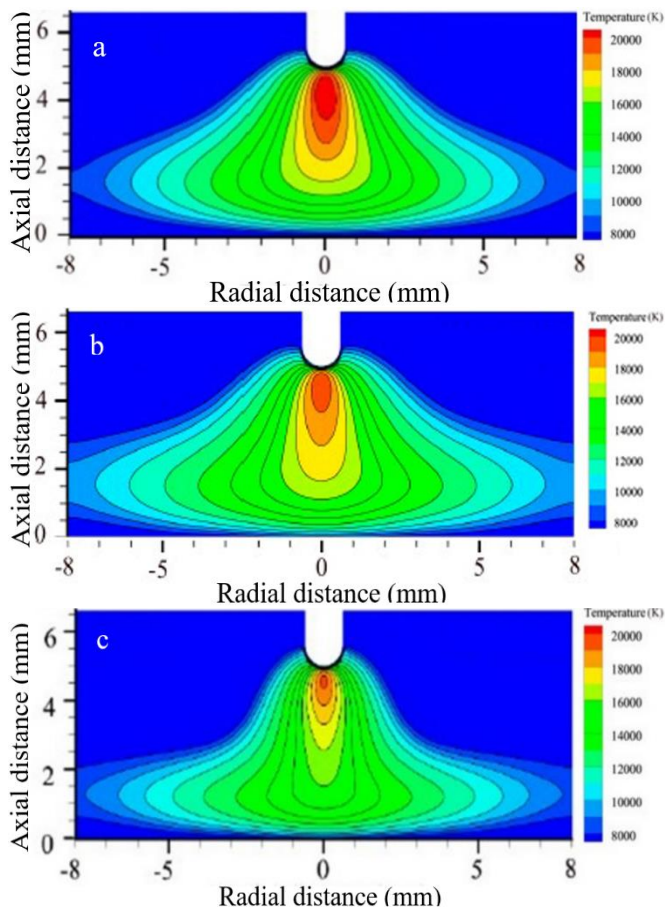


Figure 8. Arc temperature distribution of different protection gas: (a) 5% H₂ + Ar; (b) pure Ar; (c) 25% CO₂ + Ar

4. RESULTS DISCUSSION

4.1 Microstructure evolution

W1, W2, and W3 weld metals dilution percentages calculated from weld joints' geometrical characteristics ATR, ARR, ABF, AWD, and ARG illustrated in Figure 2-Eqs. (1) and (2), respectively, employed in weld metal dilution percentage estimated. Shielding gas mixtures affects welding beads' geometric, weld metal deposition area (AWD), fusion base metal area (ABF), and base metal dilution percentage (DL%), as shown in Table 3. Calculated results demonstrated that the higher AWD, ABF, and DL% were calculated in W1 with 5% H₂ + Ar shielding gas mixture then W2 with pure argon, and the last value calculated was in W3 with argon and CO₂ mixture, these results are likely because welding and shielding gas action in maintaining welding heat are influenced by the effects of a mixture of pure argon and hydrogen on the flow rate temperature of molten metal under nonuniform heating and cooling conditions. You can see it in the welding arc. The fact that welding protection gas marches downward from the electrode and nozzle is processed by it. Afterward, gas is incentivized to gather at the electrode tip. Ionized gas surrounding the electrode tip is compressed by electromagnetic forces acting radially and axially toward the

workpiece, resulting in the production of an arc plasma. The downward axial momentum of the arc plasma flow is converted into the outward radial momentum as it hits the workpiece surface, causing the plasma to flow radially outward. It is believed that pure argon gas has an axial velocity of up to 230m/s in the arc column [23]. The arc plasma and heat distribution throughout the welding zone are both improved by the Ar gas's desirable ionization characteristics, which in turn improve the qualities of the welded metal. The penetration depth of the welding zone is affected by the rise in heat concentration caused by the addition of hydrogen gas to welding protection. Because H₂ is insufficient as a welding shielding gas, the dilution percentage of the W2 sample welded with pure Ar is greater than that of W3 but lower than that of W1 welded with H₂ addition. Equivalents of chromium (Creq) and nickel (Nieq) were calculated from the equations used in the fusion metal dilution calculations. 3, and 4 were used to determine Creq/Nieq ratios. In Table 4, the computed Creq/Nieq ratios can be seen. According to Creq/Nieq ratios, weld metal solidification mode for 5% H₂ + Ar gas mixture, pure Ar, and 25% CO₂ + Ar gas mixture welding metals can be a predicate, Creq/Nieq ratios value of welding samples are 1.85, 1.81, and 1.8, based on these values and from earlier studies solidification mode will follow this category [24-26]:

FA Mode: L→L + δ→L + δ + γ→γ + δ→γ: 1:48 < Creq/Nieq < 1:95

Table 4. Dilution percentage calculation

Sample Specification	W1	W2	W3
(ABF) _{mm}	15.46	13.37	9.38
(AWD) _{mm}	32.56	30.83	24.84
DL%	47.48	43.46	37.76

However, due to the high cooling rate of the 20% CO₂ + Ar gas mixture, the final result of the weld metal will be the transformation of the austenite structure to martensite. Many publications on different shielding gases are temperature dependent, estimated assuming the equilibrium conditions of local thermodynamics. For example, these data can be found in the researches for argon and for CO₂ [27, 28]. According to earlier studies, the heating values in the protection gas nozzle area are about 300-900K. CO₂ thermal conductivity and specific heat capacity are higher than argon's in this range. This leads to a higher cooling effect of CO₂ compared with argon in this temperature range. However, no quantification of this effect can be derived from material data alone due to the influence of gas flow formation on the heat transfer mechanism. The viscosity and density of shielding gases also play a significant role. With a temperature range between 300-900K, argon viscosity is about two times more than CO₂, while CO₂ density is about 10% bigger than argon. Arc temperatures and radiated heat also vary between welding shielding gases. According to the studies of Kozakovet al. [29] and Wilhelm et al. [30], approximately 9000-10,000K temperatures of metal-vapor dominated arc core determined for pure argon shielding gas arc, and temperature in plasma was about 12,000K. CO₂ covering gas mixtures with high argon content recorded arc core temperature more than arc under pure argon shielding gas. The calculated arc temperature for 25% CO₂ with argon shielding gas mixture was 10,000K in arc core and between 11,000K and 14,000K in plasma.

FA solidification mode deeply affects welding zone microstructure phase transformations, austenite, ferrite, and

liquid three-phase reaction solidification stage plus ferrite precipitation and continuing of $\delta \rightarrow \gamma$ transformation below solidus line, all that depending on FA solidification mode [31]. δ -ferrite in welding metal measured by employing an FMP30 magnetic induction instrument, δ -ferrite would be comparable of the three welding metal solidification samples due to the simple difference in C_{req}/Ni_{eq} ratios and C_{req} , Ni_{eq} , among them as shown in Table 5. Three weld metal δ ferrite measurements indicated less than 5% variation between them. Also, the C_{req}/Ni_{eq} ratio calculation reveals that W1 weld metal having lowest value but the highest δ -ferrite content among the three joints; this is due to the highest thermal properties of H_2 in the shielding gas mixture used in the protection of welding joint, hydrogen addition also increases molten weld metal volume in joint due to H_2 gas high thermal conductivity protection gas mixtures at temperatures when hydrogen molecules dissociate [16]. Also, H_2 addition to argon increasing welding speeds which repossess welding heat source in speedy rate from and led to rapid solidification of welding metal across FA mode. Cooling rate strongly affected δ ferrite nucleation rate and its amount in welding zone microstructure; δ ferrite formation usually increases with the cooling rate increases. This ferrite will transform to austenite ($\delta \rightarrow \gamma$ transformation). Still, partial transformation (as retaining δ ferrite) will increase W1 weld δ ferrite content and toughness, the same sequence in welding zone microstructure excepted with pure Argon weldment W2. The transformation sequence in the W3 weldment sample is different due to the high cooling effect of CO_2 gas in the shielding gas mixture, which involved a significant increase in the welding zone cooling rate and undesirable transformation of austenite to martensite with a decrease in δ ferrite contains and welding zone toughness. δ ferrite is Important in welding metal microstructure because of its fundamental effects in the interception of hot cracking starting and progression in microstructure and enhanced joint resistance to hot cracking. In order to strengthen hot and solidification cracking resistances during the solidification sequence, 5-10% δ -ferrite is essentially required [32], W1 welded with 5% $H_2 + Ar$ shielding gas mixture, and W2 with pure argon δ -ferrite vol.% were 15.38, 13.17 respectively which are excellent values inprevented hot and solidification cracking through welding metal solidification. W3, which was welded with 25% $CO_2 + Ar$ shielding gas mixture δ -ferrite vol.% was 5.83; this value is very critical in preventing hot and solidification cracking through welding metal solidification, that means any sample increasing with cooling rate due to any reason will take us to solidification cracking zone issues. These results reveal that all three welded joints were preserved against cracking problems but with critical conditions with W3.

Table 5. Weld metal specification transformation (Ms and Mes) temperatures, and SFE

Specifications	W1	W2	W3
C_{req}	19.48	19.22	16.40
Ni_{eq}	10.19	10.07	10.22
C_{req}/Ni_{eq} ratio	1.911	1.908	1.604
δ -ferrite, vol.%	16.42	14.25	8.27
SFE, mJ/m ²	14.76	14.16	8.71

Strain hardening and phase transformation are strongly connected to material stacking fault energy (SFE), and the SFE values of three welding samples were calculated using the Rhodes and Thompson Eq. (7). previous studies [33, 34]

reveal that martensite transformation $\gamma \rightarrow \epsilon \rightarrow \alpha'$ is excepted when SFE is less than (9 mJ/m²). Therefore, in this study with (14.67, 14.16) SFE values for W1 and W2, as shown in Table 5, which is much higher than AISI 304 base metal with 12.5 mJ/m² SFE value, the formation of lath martensite and lath (α') is not predictable from the transformation from austenite (γ). High SFE will increase the stability of austenite (γ) phases in microstructure and hinder transformation to lath martensite by lowering M_s starting temperature, which is responsible for lath martensite formation, W3 SFE value is thoroughly demonstrated different derivation, the SFE value of W3 is less than (9 mJ/m²) that is mean martensite microstructure will form in solidified welding zone microstructure, Table 5 results shown SFE relation with C_{req}/Ni_{eq} ratio and pointed out the SFE value decreasing with C_{req}/Ni_{eq} ratio lowering as shown in Figure 9.

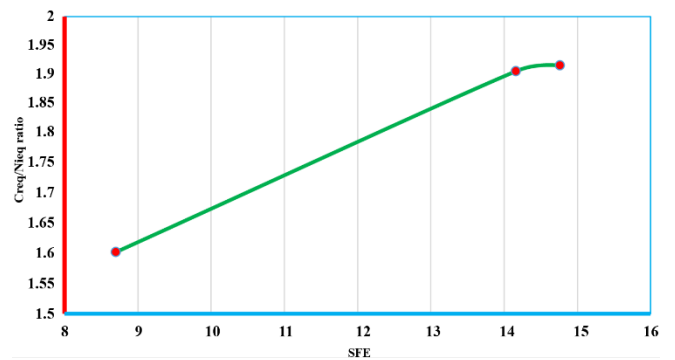


Figure 9. Relation between SFE and C_{req}/Ni_{eq} ratio for the three welded joints

4.2 Welded microstructure optical micrographs and SEM evolution

Austenite (γ) with ferrite (δ) existence after completed solidification can be observed in optical micrographs of the W1 sample, which represents weldment with 5% $H_2 + Ar$ in Figure 4(a), and W2, which is welded with pure Argon in Figure 5(a). Fusion zone microstructure reveals an austenitic matrix with two types of δ -ferrite, skeletal δ -ferrite and lathy. W1 microstructure showed a higher concentration of lathy δ -ferrite type in welding metal microstructure from W2 and W3 due to the H_2 gas's high thermal conductivity; W3 microstructure in Figure 6(a) shows martensite in weld metal microstructure due to cooling effects of CO_2 in protection gas mixture which increasing cooling rate and resulted in austenite transformation to martensite. According to the pseudobinary phase diagram and weldment sample compositions, the solidification mode of all welding metals belongs to the ($\gamma + \delta$) two-phase solidification zone. According to the C_{req}/Ni_{eq} ratio, eld metal compositions have a markable effect in δ -ferrite formation. David et al. [35] investigation study demonstrated that when the C_{req}/Ni_{eq} ratio is less than 1.35, weld metal solidification ends with austenite. When the ratio is more than 1.35, solidification will end with ferrite. Based on the values in Table 5, all weld metal joints had a C_{req}/Ni_{eq} ratio of more than 1.35, and it will solidify in ferritic/austenitic mode; because of the strong cooling effects of CO_2 welding sample, W3 would solidify as martensite.

Ferrite to austenite transformation during stainless steel welding is a progressive process governed by elements' diffusion and cooling rate; in the welding process, this transformation is incomplete due to the rapid cooling rate

compound with welding, the austenite growth during the transformation causes rejection of Cr from structure and Ni absorption, this process causes high Cr concentration and Ni depletion in residual ferrite [36]. Because of elements diffusion affected by cooling rate, stainless steel welding suffered from uncompleted transformation of ferrite to austenite. as illustrated in Figures 4(a) and 5(a) welding zone final microstructure of W1 and W2 samples is dendrite cores with retained skeletal δ -ferrite, this due to transformation of thinner lamellae ferrite to austenite in solidification during cooling process, while thicker texture with primary dendritic ferrite suffers from incompletely dissolved issues and retained as skeletal δ -ferrite in dendrite cores, final microstructure of weld metal in W3 as illustrated in Figure 6(a) shown martensite microstructure with needle shape as a result of very fast cooling rate in W3 weld metal solidification due to cooling effects of CO₂ in shielding gas mixture used with W3, very fast cooling rate caused ferrite transformation to austenite with almost entirely transformation with very limited retained ferrite in microstructure, which explain the low ferrite measuring with W3 sample. This austenite is transformed into martensite when it undergoes the cooling effects of CO₂ gas. Examination of the welding zone microstructure in Figure 4(a) reveals that W1 weld metal has the highest heat concentration because of H₂ gas effects and the highest temperature gradient across the welding zone and HAZ (highest degree of supercooling). These sequences hinder austenite stabilizing elements' diffusion during ferrite transformation to austenite in welding metal microstructure. Without the diffusion of these elements, microstructure finally results in lathy δ ferrite creation along with δ ferrite skeletal morphology [37]. Optical micrographs of microstructure in Figure 4(b) and Figure 4(b) illustrate the W1 and W2 welding fusion boundary (FB) and high-temperature heat affected zone (HTHAZ) formation with sensitization zone along the fusion line. HTHAZ was created adjacent to the welding fusion line when the parent metal temperature rose above A3 temperature (910°C) during welding, and it was described as an austenite grain structure with martensite at the grain's boundary. However, the martensite amount is insufficient to restrict grain enlarging across HTHAZ. W3 weldment sample shows HTHAZ with smaller grains from W1 and W3 due to the cooling effects of CO₂ gas, but it's still large; this enhancement in HAZ was deleted by the formation of martensite microstructure in the welding zone.

Because of this, grain size coarsening in general controlled HTHAZ despite solid-state phase partial transformation during cooling weld metal. The grain sizes of W1 and W2 are much the same, with a small difference in W3 due to a slight difference in the amount of heat input (Table 3). Carbide precipitation on the grain boundary can be detected as narrow and tight with no more than a few μm and a dark appearance sensitization region along the fusion line. Carbide precipitation occurred because of dendritic growth and solidification of primary ferrite from liquid welding metal during the cooling of HTHAZ, which is adjacent to the welding fusion line. Alloying elements like chromium, nitrogen, carbon, and nickel reinforced the interdendritic liquid just before complete welding metal solidification due to the segregation of C, N, and Ni from ferrite to the surrounding liquid. Because of the austenitic stabilizing elements concentration, the remaining liquid solidified in γ -phase and δ / δ interfaces, which are considered powerful site carbide and nitride precipitations (particularly MX and M₂₃C₆ type).

Mainly, carbide precipitations like Cr₂₃C₆ and Cr₂N can occur along grains boundary adjacent to the fusion line due to cooling time in this zone; for these reasons, W3 sample demonstrated carbide precipitations or sensitization regions much more significant than what founded in W1 and W2 due to the fast cooling time which did not allow Cr to redistributed in microstructure and redissolved from its carbides, this region suffered from the heating flow in longitudinal direction from heating source over welding center line across HTHAZ and base metal stay within temperature range between 900 to 400°C for long time enough to carbide precipitations [37]. These precipitations formed a continuous sensitized region and expanded cooling time. The alloy segregation generated coarse austenite grain's structure next to the sensitization zone, according to coarse austenite grain's structure, which resulted in precipitation lack and unwanted phase transformation; this zone expiated to where the weldment failure under pressure or tensile force.

4.3 Welded microstructure SEM evolution

SEM examination of welding metals Figures 7(a)-(c) was performed to test tiny microstructure details. SEM observations confirmed the lath and skeletal formation like embedded ferrite structure at austenite matrix as intergranular δ ferrite. Figures 7(a) and (b) reveal W1 weld metal and W2 δ -ferrite intergranular formation nature and show high lath δ ferrite constraints in W1 welding metal more than W2 also confirm needle microstructure morphology of martensite with gas porosity in W3 as shown in Figure 7(c). Also, SEM analysis of W1 weld metal and W2 is evident that welding metals do not undergo any solid-state phase transformation (i.e., $\gamma \rightarrow \delta \rightarrow \alpha'$). This is due to ferrites' arms, which build lattices in an austenite grain; the austenite in this lattice will present a homogeneous and high dislocation density. Also, this action results in weld metals with structures showing high SFEs and very low MT temperatures, which enhance the γ -phase stability during cooling and restricted phase transformation. SEM analysis of W3 weld metal welding shows that the weld metal undergoes higher cooling than W1 and W2, and solid-state phase transformation (i.e., $\gamma \rightarrow \delta \rightarrow \alpha'$) to martensite occurred in microstructure due to CO₂ cooling effects. Welding heat concentration in the W1 welding sample because of the thermal conductivity of H₂ in shielding gas influenced the welding pool in two different ways simultaneously. The welding heat concentration strongly affects Lorentz or electromagnetic force in welding molten metal due to increased localized heat concentration with current. Also, the proper WS is essential with high heat concentration because it tends to decrease the Marangoni force. This compensation of low Marangoni and high Lorentz force caused penetration with finger shape, developing strong downhill molten metal flow and controlling grain growth.

4.4 Microstructure effect on mechanical properties

Different weldment zones' Vickers micro-hardness average values are recorded in Table 6 and illustrated in Figure 10; base metal, HAZ, and fusion boundaries' micro-hardness average values were recorded for the three shielding gas mixture weldments. Micro hardness tests demonstrated maximum hardness found in welding metal and little drop in HAZ, but a markable drop in hardness was observed in fusion boundaries, as shown in Table 5. The W3 sample with CO₂

and argon mixture showed the highest hardness in the welding zone and fusion boundary due to martensite formation in the welding zone and carbide precipitation in the fusion boundary. It had a very high cooling rate in this sample.

Table 6. Vickers microhardness values for different welding zones transformation (Ms and Mes) temperatures, and SFE

Weldment No.	Weld Metal	Fusion Bounders	HAZ	Base Metal
W1	237.125	206	222.25	207.22
W2	230.75	200.5	218.125	203.30
W3	248.3	215.5	231.75	201.35

The highest microhardness value from Table 5 and Figure 10 was recorded in W3 weld metal with a 25% CO₂ + Ar mixture; this is because the martensite microstructure formation in this zone resulted from the very high cooling rate, W3 fusion boundaries (FB) zone suffered from carbide precipitation. Still, this area showed finer grain size from the welding zone, reducing this zone's hardness. W2 sample with 5% H₂ + Ar mixture welding zone illustrated microhardness values less than W3 but higher than W1 due to the formation of microstructure without any evidence about martensite formation and fine grain size with high angle grains boundaries, which restricted dislocations movements like this structure. W2 fusion boundaries (FB) and the zone close to it showed a significant decrease in microhardness because of the depletion of refiner elements toward the HAZ and phase transformation in this zone, which caused grains to enlarge in this region. Sample welded with pure Ar shielding gas showed a very close value to the W2 sample but less than W2 due to the larger grain size in the welding zone compared with the W2 welding zone grain size because of the lack of heat constation provided by H₂ addition in the W2 sample. HAZ micro-hardness, as shown in Table 5, is higher than the parent metal and fusion boundary but less than the welding zone in all three samples; HAZ region formation of undiluted 304 parent metal and suffered from heating above 910°C which is recognized as A3 temperature, 304 stable austenite, when heated above the A3 region, partially transforms into martensite during the cooling process if the cooling rate is fast enough for this transformation (i.e., $\gamma \rightarrow \epsilon \rightarrow \alpha'$). This transformation occurs accompanied by residual stress and thermal field formation. This transformation creation HAZ with γ phase and martensite in grain boundary provides higher hardness than FB and parent metal.

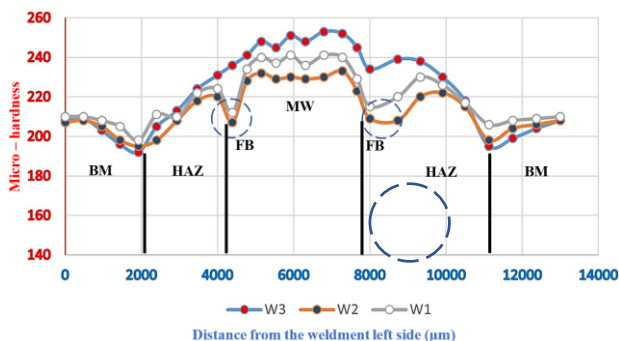


Figure 10. Micro-hardness across weldments

4.5 Tensile test and deformation behaviour

According to ASTM E8 code, as mentioned by earlier

studies, three tensile test samples were prepared for each protection gas mixture, with dimensions as shown in Figure 3; the average test results of three samples shown in Table 7, W1 and W2 samples failed in fusion boundary as demonstrated in Figure 11 which evidence that this region is much weaker than welded metal zone and HAZ. In contrast, the W3 sample failed in the welding zone due to its high hardness resulting from martensite formation; these results concur with the microstructure and microhardness in the previous analysis. Table 6 shows that the W1 tensile sample illustrated higher UTS and elongation than the W2 and W3 samples. Differences in strength characterized between the three samples are strongly related to microstructure and texture alteration resulting from heating characterization and consternation due to welding protection gas effects and their impacts on the cooling rate. The tensile test mechanism caused the BCC phase to increase in the austenite matrix, and the formation of the BCC structure in the FCC matrix was expected; transformation over tensile test deformation preferred α' (BCC). According to earlier research [38], γ phase transformation to α' phase is a consecutive process and is expected to take this order:

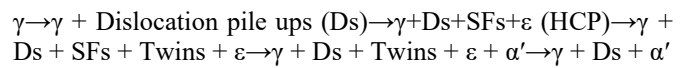


Table 7. Welding joints tensile results

Sample	(YS) MPa	(UTS) MPa	(Load at UTS) kN	Elongation%	Fracture Location
W1	342	618	14.31	45.30	FB
W2	336	599	14.20	42.17	FB
W3	326	569	14.02	39.24	WZ

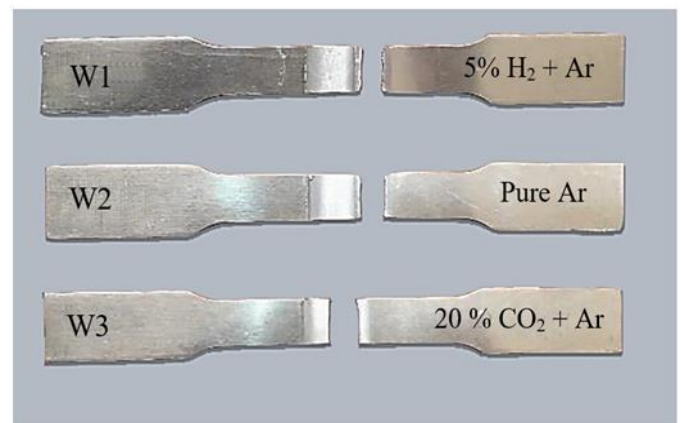


Figure 11. Failure location in three samples

The highest tensile value of the W1 sample is evident that the W1 sample microstructure has the finest grain size among the three samples as a result of the most increased heat characterization of H₂ addition to the welding protection gas; these analyses can be proved with microhardness values, like this microstructure in W1 and W2 samples, naturally consists of high angle grains boundary HABs in high concentration usually much higher than low grains boundary LABs concentration. The high density of HABs restricts dislocations traveling through the interface, which transport plastic deformation slips in materials. Dislocation's activities are the creator of twinning structure, which subsequently firmly rearrangement the partial dislocations, which are precursors of HCP and ϵ -martensite structure starting. Previous studies in

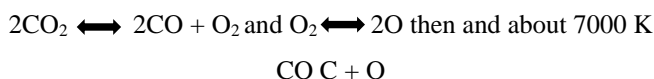
stacking faults principles (SFs) proposed that FCC twinning and FCC-HCP structure transformation are strongly related to the dislocation density in microstructure [39]. The low value of (SFs) in W3 and martensite microstructure formation strongly agreed with these results, which showed the lowest mechanical properties among the three samples. W1 microhardness values, which were higher than W2 results, illustrated dislocation movement resistance across the structure due to HABs in W1 weld metal microstructure, which caused accumulation of dislocation at the grain boundary and increased stress and hardness. W2 results show different situations: reduction in strength evidenced by microstructure with LABs concentration higher than W1 reflected impedance in dislocation movements hindering across the grain boundary, microstructure with a high percentage of LABs unable to excited the initial stage of dislocation pile-ups which finally postpone transformation concatenation.

In the W3 welding sample, SFs low value enhanced HCP structure formation condition on γ , and the twin structure creation on the closest packed γ plane of FCC crystal [40]. ϵ phase or twinning structure considerably influenced the intermediate phase in γ to α' martensite transformation structure. Also, earlier studies have proved that the ϵ -martensite intersections or twinning deformation are favorable to α' -martensite nucleation phenomena [41]. Highly concentrated locations always consider MT originates, while the prominent distortion location triggered the embryo nucleation and growth of α' crystal along the primary slip plane of ϵ -phase. Increasing dislocation density and strain energy accumulation are strongly connected to martensite creation in microstructure, and martensite growth is related to volume fraction expansion and phase transformation [41].

For all these reasons, the strength and elongation of welding metal are determined by the higher dislocation accumulation, SFs, twinning deformation, and strain hardening-induced martensite.

4.6 Arc heat flux density distribution model

From Eqs. (6)-(8), with fixed welding parameters for all weldments, the η_h value is connected to k and q_{max} values. As shown in Figure 8, H_2 addition to argon in welding protection gas increasing q_{max} . Welding arc heat flux density increases with H_2 addition due to two factors. First, H_2 content lowers the electrical conductivity below 20,000K, resulting in currents flowing closer to the arc axis and producing more arc-constricted central regions with higher temperatures [42]. Second, increasing thermal conductivity enhanced the conductive heat transfer from the welding arc to the workpieces. An increase in thermal conductivity also resulted in the expansion of the welding arc and the transfer of conductive heat to the plate; this would slightly decrease the value of K . Therefore, according to Eq. (8), H_2 addition would increase the welding heat efficiency. CO_2 gas has a triatomic structure, which separates in the upper welding arc and combines again near the welding pool surface. CO_2 gas breaking and recombination resulted in prominent peaks in thermal and specific heat conductivity at breaking temperatures of about 3500K according to the following reactions:



As a result of the energy consumed by CO_2 gas to dissociate, arc temperature will decrease if power stays constant. At dissociation temperatures, thermal conductivity peaks increased with conductive heat transfer to the workpiece plate. Increased CO_2 content with an appropriate amount can increase q and η_h values. However, when CO_2 addition is more than (20%), the welding arc temperature is lower, the arc besieges firmly, and the area around the arc axis suffers from more heat concentration. Therefore, q_{max} increases, and k also increases. The fundamental increase of the k value resulted in η_h decrease despite q_{max} increasing.

Welding joint geometrical dimensions are also affected by protection gas composition. With H_2 addition, the arc heat flux density increases, so joint geometrical parameters increase in theory. However, welding arc length is assumed constant in numerical simulation for different shielding gases. Still, in the actual gas metal arc welding process, the arc length decreases with the H_2 or CO_2 additions to stabilize the voltage [43]. Arc length decreases are influenced by reducing arc root area. Therefore, welding arc heat transfer properties and the arc length affect joints' geometrical parameters.

5. CONCLUSIONS

Research results illustrated that welding shielding gas has an essential effect on heating concentration and focusing, which affects base metal with filler dilution percentage, which controls δ -ferrite contain variation in austenite matrix-skeletal and lathy δ -ferrite microstructure observed in W1 and W2 welding zone microstructure. The results also showed weld metal microstructure in W1 with high lathy δ ferrite concentration, while W2 illustrated almost the same microstructure of W1 but with less concentration of lathy δ ferrite. Martensite formation was detected in the W3 welding zone microstructure with an apparent needle shape.

SEM morphology also demonstrated skeletal and lathy δ -ferrite embedded in austenite matrix like intergranular and intragranular δ -ferrite. SEM examination manifests no $\gamma \rightarrow \epsilon \rightarrow \alpha'$ phase transformation takes place in weld metals of W1 and W2 welding samples during cooling. W3 SEM examination showed needle martensite formation with gas porosity due to the high cooling rate of the welding zone. Coarse grain size HTHAZ formation adjacent to the fusion line at the fusion boundaries can be observed in optical micrograph examination. FB optical micrographs also illustrated the dark appearance of a narrow-sensitized zone along the welding fusion line; carbide precipitation like M23C6 and MX type in the grain boundary is probably the reason for this formation. Austenite structures with coarse grains can also be detected at the fusion zone, just next to the sensitization region, due to the prolonged cooling time and alloy segregation in this region. This coarse grain structure and sensitized zone at the fusion boundary create a fragile zone compared with the surrounding structure and cause failure in this region during a tensile test of W1 and W2 weldments.

Microstructure examination of weld metal W1 shows the finest structure compared to W2 and W3. The effects of this fine microstructure are reflected clearly in microhardness values, in general. For all three weldments, the microhardness test data shows that the weld metal has the highest values, and also, the data display functional lack in the fusion boundary zone; the HAZ in this experiment showed relatively higher hardness from base metal and fusion boundary but less than

welding zone metal, W1 reveal the highest hardness values then W2 and finally W3. Tensile test results showed that W1 weldment has higher elongation and strength than W2 and W1, and all three samples failed in FB. The W1 tensile test results reflected the effects of the fine grain microstructure, which naturally produced high HAB density, impeded the dislocation movements across the interface, and attributed to higher dislocation pile-ups. This action enhances strain energy absorption and accumulation of FCC twins and ϵ -phases transformation process, which act like an intermediate phase in γ to α' transformation. For these reasons, factors that determined elongation and tensile strength of welding metal attributed to high dislocation pile-ups, SFs, twinning deformation, and strain hardening induce martensite.

In conclusion, this study's findings provide crucial evidence that welding shielding gas significantly affects weld joint properties and the overall welding process. This is because the gas influences grain size and microstructure type, just as heat concentration and cooling rate impact the type and mechanism of welding metal phase transformation. The welding arc's properties and, by extension, its heat source, were affected by the welding protection gas's composition. Paying close attention. Adding hydrogen to argon improves heat efficiency by raising the heat concentration factor. Even if the maximum heat flux density increases, the arc heat efficiency falls due to the heat constriction factor caused by CO₂ levels of more than 20%. The composition of the shielding gas also affects the joint's geometrical properties. Due to a decrease in welding arc length and an increase in the geometrical features of the joint, focused heat is transmitted to the welding region with the addition of H₂. Joint geometrical parameters are impacted as well and the CO₂ component surpasses 20% because arc heat constricts and arc length reduces. For future research directions, an investigation about the inter-pass temperature and the pre-heat and post-heat treatment effects on welding joint mechanical properties could be investigated.

REFERENCES

- [1] Takuda, H., Mori, K., Masachika, T., Yamazaki, E., Watanabe, Y. (2003). Finite element analysis of the formability of an austenitic stainless steel sheet in warm deep drawing. *Journal of Materials Processing Technology*, 143: 242-248. [https://doi.org/10.1016/S0924-0136\(03\)00348-0](https://doi.org/10.1016/S0924-0136(03)00348-0)
- [2] Cary, H.B., Helzer, S.C. (2005). *Modern Welding Technology*. Pearson/Prentice Hall, USA.
- [3] Castro, H., Rodriguez, C., Belzunce, F.J., Canteli, A.F. (2004). Mechanical properties and corrosion behaviour of stainless steel reinforcing bars. *Journal of Materials Processing Technology*, 143: 134-137.
- [4] Lothongkum, G., Chaumbai, P., Bhandhubanyong, P. (1999). TIG pulse welding of 304L austenitic stainless steel in flat, vertical and overhead positions. *Journal of Materials Processing Technology*, 89: 410-414. [https://doi.org/10.1016/S0924-0136\(99\)00046-1](https://doi.org/10.1016/S0924-0136(99)00046-1)
- [5] Jha, A.K., Arumugham, S. (2001). Metallographic analysis of embedded crack in electron beam welded austenitic stainless steel chemical storage tank. *Engineering Failure Analysis*, 8(2): 157-166. [https://doi.org/10.1016/S1350-6307\(00\)00003-0](https://doi.org/10.1016/S1350-6307(00)00003-0)
- [6] Richard, S.S. (1995). *The Procedure Handbook of Arc Welding*. The Lincoln Electric Company.
- [7] Gülenç, B., Develi, K., Kahraman, N., Durgutlu, A. (2005). Experimental study of the effect of hydrogen in argon as a shielding gas in MIG welding of austenitic stainless steel. *International Journal of Hydrogen Energy*, 30(13-14): 1475-1481. <https://doi.org/10.1016/j.ijhydene.2004.12.012>
- [8] Boiko, I., Avisans, D. (2013). Study of shielding gases for MAG welding. *Materials Physics and Mechanics*, 16(3): 126-134.
- [9] Taban, E., Kaluc, E., Aykan, T.S. (2014). Effect of the purging gas on properties of 304H GTA welds. *Welding Journal*, 93(4): 124-130.
- [10] Salleh, M.S., Ramli, M.I., Yahaya, S.H. (2011). Study on mechanical properties and microstructure analysis of AISI 304L stainless steel weldments. *Journal of Mechanical Engineering and Technology (JMET)*, 3(2): 71-82. <http://doi.org/10.2022/jmet.v3i2.374>
- [11] Kishore, K., Krishna, P.G., Veladri, K., Ali, S.Q. (2010). Analysis of defects in gas shielded arc welding of AISI1040 steel using Taguchi method. *ARPN Journal of Engineering and Applied Sciences*, 5(1): 37-41.
- [12] Palani, P.K., Murugan, N. (2006). Selection of parameters of pulsed current gas metal arc welding. *Journal of Materials Processing Technology*, 172(1): 1-10. <https://doi.org/10.1016/j.jmatprotec.2005.07.013>
- [13] Utkarsh, S., Neel, P., Mahajan, M.T., Jignesh, P., Prajapati, R.B. (2014). Experimental investigation of MIG welding for ST-37 using design of experiment. *International Journal of Scientific and Research Publications*, 4(5): 1.
- [14] Tusek, J., Suban, M. (2000). Experimental research of the effect of hydrogen in argon as a shielding gas in arc welding of high-alloy stainless steel. *International Journal of Hydrogen Energy*, 25(4): 369-376. [https://doi.org/10.1016/S0360-3199\(99\)00033-6](https://doi.org/10.1016/S0360-3199(99)00033-6)
- [15] Althouse, A.D., Turnquist, C.H., Bowditch, W.A., Bowditch, K.E. (2018). *Gas Tungsten Arc Welding: Modern Welding*. Goodheart-Willcox, 327-328.
- [16] Lowke, J.J., Morrow, R., Haidar, J., Murphy, A.B. (1997). Prediction of gas tungsten arc welding properties in mixtures of argon and hydrogen. *IEEE Transactions on Plasma Science*, 25(5): 925-930. <https://doi.org/10.1109/27.649597>
- [17] Ha, X.H., Jang, S.W., Bang, W.H., Yoon, U.S., Oh, K.H. (2002). Texture evolution in weld regions of SUS-304 stainless steel and TRIP steel. *Materials Science Forum(Switzerland)*, 408(2): 1377-1382.
- [18] Kotecki, D.J. (2000). A martensite boundary on the WRC-1992 diagram-part 2: The effect of Manganese. *Welding Journal*, 79(12): 346-354.
- [19] Dai, Q.X., Cheng, X.N., Zhao, Y.T., Luo, X.M., Yuan, Z.Z. (2004). Design of martensite transformation temperature by calculation for austenitic steels. *Materials Characterization*, 52(4-5): 349-354. <https://doi.org/10.1016/j.matchar.2004.06.008>
- [20] Durgutlu, A. (2004). Experimental investigation of the effect of hydrogen in argon as a shielding gas on TIG welding of austenitic stainless steel. *Materials & Design*, 25(1): 19-23. <https://doi.org/10.1016/j.matdes.2003.07.004>
- [21] Durgutlu, A., GÜLENÇ, B. (1999). The effect of welding speed on the microstructure and penetration in arc welding Article Ark kaynagında kaynak hizinin nufuziyete ve mikroyapıya etkisi. *Turkish Journal of*

- Engineering and Environmental Sciences, 23(4): 251-259.
- [22] Qu, X.S., Qin, C.H., Sun, G.J., Xie, Y.N. (2022), Research on fracture of steel structure welded joint based on micro-mechanism. *Structures*, 43: 434-448. <https://doi.org/10.1016/j.istruc.2022.06.048>
- [23] Hu, J., Tsai, H.L. (2007). Heat and mass transfer in gas metal arc welding. Part I: The arc. *International Journal of Heat and Mass Transfer*, 50(5-6): 833-846. <https://doi.org/10.1016/j.ijheatmasstransfer.2006.08.025>
- [24] Lee, J.H., Kim, H.C., Jo, C.Y., Kim, S.K., Shin, J.H., Liu, S., Trivedi, R. (2005). Microstructure evolution in directionally solidified Fe-18Cr stainless steels. *Materials Science and Engineering: A*(413): 306-311. <https://doi.org/10.1016/j.msea.2005.09.021>
- [25] Pryds, N.H., Huang, X. (2000). The effect of cooling rate on the microstructures formed during solidification of ferritic steel. *Metallurgical and Materials Transactions A*(31): 3155-3166. <https://doi.org/10.1007/s11661-000-0095-1>
- [26] Elmer, J.W., Allen, S.M., Eagar, T.W. (1989). Microstructural development during solidification of stainless steel alloys. *Metallurgical Transactions, A*(20): 2117-2131. <https://doi.org/10.1007/BF02650298>
- [27] Murphy, A.B., Arundell, C.J. (1994). Transport coefficients of argon, nitrogen, oxygen, argon-nitrogen, and argon-oxygen plasmas. *Plasma Chemistry and Plasma Processing*, 14: 451-490. <https://doi.org/10.1007/BF01570207>
- [28] Yang, A., Liu, Y., Sun, B., Wang, X., Cressault, Y., Zhong, L., Rong, M., Wu, Y., Niu, C. (2015). Thermodynamic properties and transport coefficients of high-temperature CO₂ thermal plasmas mixed with C₂F₄. *Journal of Physics D: Applied Physics*, 48(49): 495202. <https://doi.org/10.1088/0022-3727/48/49/495202>
- [29] Kozakov, R., Gött, G., Schöpp, H., Uhrlandt, D., Schnick, M., Häßler, M., Füssel, U., Rose, S. (2013). Spatial structure of the arc in a pulsed GMAW process. *Journal of Physics D: Applied Physics*, 46(22): 224001. <https://doi.org/10.1088/0022-3727/46/22/224001>
- [30] Wilhelm, G., Kozakov, R., Gött, G., Schöpp, H., Uhrlandt, D. (2012). Behaviour of the iron vapour core in the arc of a controlled short-arc GMAW process with different shielding gases. *Journal of Physics D: Applied Physics*, 45(8): 085202. <https://doi.org/10.1088/0022-3727/45/8/085202>
- [31] Li, J.Y., Sugiyama, S., Yanagimoto, J. (2005). Microstructural evolution and flow stress of semi-solid type 304 stainless steel. *Journal of Materials Processing Technology*, 161(3): 396-406. <https://doi.org/10.1016/j.jmatprotec.2004.07.063>
- [32] Kou, S. (2003). *Welding Metallurgy*. John Wiley & Sons, Inc.
- [33] Seetharaman V, Krishnan R. (1981) Influence of the martensitic transformation on the deformation behaviour of an AISI 316 stainless steel at low temperatures. *Journal of Materials Science*, 16: 523-530.
- [34] Tavares, S.S.M., Neto, J.M., da Silva, M.R., Vasconcelos, I.F., de Abreu, H.F.G. (2008). Magnetic properties and α' martensite quantification in an AISI 301LN stainless steel deformed by cold rolling. *Materials Characterization*, 59(7): 901-904. <https://doi.org/10.1016/j.matchar.2007.07.007>
- [35] David, S.A., Vitek, J.M., Reed, R.W., Hebble, T.L. (1987). Effect of rapid solidification on stainless steel weld metal microstructures and its implications on the Schaeffler diagram. Oak Ridge National Lab. (ORNL), Oak Ridge, TN (United States). <https://doi.org/10.2172/5957599>
- [36] Ma, J.C., Yang, Y.S., Tong, W.H., Fang, Y., Yu, Y., Hu, Z.Q. (2007). Microstructural evolution in AISI 304 stainless steel during directional solidification and subsequent solid-state transformation. *Materials Science and Engineering: A*, 444(1-2): 64-68. <https://doi.org/10.1016/j.msea.2006.08.039>
- [37] Lippold, J.C., Kotecki, D.J. (2005). *Welding Metallurgy and Weldability of Stainless Steels*. Wiley, New Jersey, p 82-86
- [38] Shen, Y.F., Li, X.X., Sun, X., Wang, Y.D., Zuo, L. (2012). Twinning and martensite in a 304 austenitic stainless steel. *Materials Science and Engineering: A*, 552: 514-522. <https://doi.org/10.1016/j.msea.2012.05.080>
- [39] Lee, E.H., Byun, T.S., Hunn, J.D., Yoo, M.H., Farrell, K., Mansur, L.K. (2001). On the origin of deformation microstructures in austenitic stainless steel: Part I- microstructures. *Acta Materialia*, 49(16): 3269-3276. [https://doi.org/10.1016/S1359-6454\(01\)00193-8](https://doi.org/10.1016/S1359-6454(01)00193-8)
- [40] Olson, G.B., Cohen, M. (1976). A general mechanism of martensitic nucleation: Part I. General concepts and the FCC \rightarrow HCP transformation. *Metallurgical Transactions A*(7): 1897-1904. <https://doi.org/10.1007/BF02659822>
- [41] Ding, H., Ding, H., Song, D., Tang, Z.Y., Yang, P., Hardening, S. (2011). Behaviour of a TRIP/TWIP steel with 18.8% Mn. *Science and Engineering*, 528(3): 868-873. <https://doi.org/10.1016/j.msea.2010.10.040>
- [42] Murphy, A.B., Tanaka, M., Tashiro, S., Sato, T., Lowke, J.J. (2009). A computational investigation of the effectiveness of different shielding gas mixtures for arc welding. *Journal of Physics D: Applied Physics*, 42(11): 115205. <https://doi.org/10.1088/0022-3727/42/11/115205>
- [43] Cai, X., Fan, C., Lin, S., Yang, C., Ji, X., Hu, L. (2017). Effects of shielding gas composition on arc characteristics and droplet transfer in tandem narrow gap GMA welding. *Science and Technology of Welding and Joining*, 22(5): 446-453. <https://doi.org/10.1080/13621718.2016.1253535>